



## ISTITUTO NAZIONALE DI RICERCA METROLOGICA Repository Istituzionale

Modeling Amorphous-Core Inductors up to Magnetic Saturation

*Original*

Modeling Amorphous-Core Inductors up to Magnetic Saturation / Ravera, Alessandro; Oliveri, Alberto; Lodi, Matteo; Beatrice, Cinzia; Ferrara, Enzo; Fiorillo, Fausto; Storace, Marco. - In: IEEE TRANSACTIONS ON POWER ELECTRONICS. - ISSN 0885-8993. - 40:1(2024), pp. 1563-1576. [10.1109/tpel.2024.3463803]

*Availability:*

This version is available at: 11696/82799 since: 2025-01-10T18:01:05Z

*Publisher:*

Institute of Electrical and Electronics Engineers Inc.

*Published*

DOI:10.1109/tpel.2024.3463803

*Terms of use:*

This article is made available under terms and conditions as specified in the corresponding bibliographic description in the repository

*Publisher copyright*

(Article begins on next page)

# Modeling Amorphous-Core Inductors up to Magnetic Saturation

Alessandro Ravera<sup>ID</sup>, *Student Member, IEEE*, Alberto Oliveri<sup>ID</sup>, *Member, IEEE*, Matteo Lodi<sup>ID</sup>, *Member, IEEE*, Cinzia Beatrice<sup>ID</sup>, Enzo Ferrara<sup>ID</sup>, Fausto Fiorillo<sup>ID</sup>, and Marco Storace<sup>ID</sup>, *Senior Member, IEEE*

**Abstract**—In power supplies, inductors operating in partial magnetic saturation are increasingly exploited, to increase power density and efficiency. The design and simulation of converters exploiting nonlinear magnetic components require accurate models, able to predict their voltage/current characteristics and power losses under different operating conditions. In practical applications, inductors are subjected to either square-wave or sinusoidal voltages with different amplitude, frequency, and duty cycle. We focus on amorphous-core inductors, characterized by an extremely soft magnetic behavior and reduced magnetic losses, with a weak temperature dependence. We propose a novel behavioral circuit model with some temperature-dependent parameters, composed of two coupled nonlinear inductors and linear resistors; a capacitor is also included to account for parasitic capacitances occurring at higher frequencies for the winding. The model is tested on two amorphous-core inductors. Good accuracy is obtained in reproducing the inductor current (with different dc biases) and power loss, for sinusoidal, square, and triangular voltages with different amplitudes (also leading to magnetic saturation), frequencies (from 25 to 200 kHz), and temperatures (from 23 to 100 °C).

**Index Terms**—Amorphous core, magnetic saturation, nonlinear circuit model, power inductor.

## I. INTRODUCTION

**P**OWER inductors are often the largest and bulkiest components in electronic switching converters. To obtain a desired inductance value, if the magnetic core area is reduced, it is necessary to increase the number of turns. This, however, induces a higher magnetization of the core, possibly approaching magnetic saturation. In this case, the behavior of the inductor is strongly nonlinear, and the inductance drops as the current increases. The approach to magnetic saturation was traditionally avoided for both the lack of appropriate inductor models and the increase of the power loss at high currents. However, the request

for higher power density is pushing researchers to demystify saturation in several applications. Recent works investigate and exploit saturation to sensibly increase the power density and, in some cases, also the efficiency of dc–dc converters [1], [2], [3], [4], [5] and inverters [6], [7], [8]. A survey on the application of saturating inductors in power supplies is given in [9].

Accurate nonlinear inductor models are necessary to predict the inductor inductance and power loss in different operating conditions. In dc–dc converters, the inductor voltage is typically a square wave signal with variable amplitude, frequency, and duty cycle, depending on the application. By contrast, when used inside an inverter, the inductor is subjected to sinusoidal voltages. The datasheets of commercial inductors provide a very detailed characterization of the component (inductance, losses, and temperature rise) for a wide range of frequencies, assuming a *linear* behavior. In some cases, SPICE models are also provided, to be included in circuit simulators. However, a full inductor characterization in the saturation region is not provided. Only inductance versus current plots at some temperatures are available, usually obtained by applying to the inductor small-amplitude sinusoidal signals, very different from the real ones. For custom-made inductors, one should refer to the datasheet of the core material, where several graphs are available [10], which do not allow, however, to obtain mathematical models valid in several operating conditions.

Space-time models based on field simulations (possibly resorting to 3-D finite-element analysis that solves Maxwell's equations) allow computing the 3-D electric, magnetic and thermal field patterns within inductors, providing inductance, detailed core loss data, winding proximity losses, and other relevant features as aggregate information. In this framework, some models of saturating ferrite-core inductors have been proposed [11], [12]. Unfortunately, these techniques are computationally quite heavy and require the knowledge of some geometric and magnetic properties, which are often undisclosed for commercial inductors.

As an alternative, circuit (behavioral) models characterize the component based on voltage–current measurements at its terminals. These models are more suitable to be embedded within circuit simulators to design, numerically emulate, and control circuits containing magnetic components, such as power converters. In this article, we focus on this second category of models.

The behavioral models surveyed in [13] and [14] are specific for low-power dc–dc converter applications because only

Received 22 March 2024; revised 28 June 2024 and 20 August 2024; accepted 12 September 2024. Date of publication 18 September 2024; date of current version 12 December 2024. This work was supported in part by the European Union - NextGenerationEU, within the project “MAGSAT - Exploiting Magnetic SATuration to increase power density in switching converters.” University of Genoa, Italy. Recommended for publication by Associate Editor H. Wang. (Corresponding author: Alberto Oliveri.)

Alessandro Ravera, Alberto Oliveri, Matteo Lodi, and Marco Storace are with the Dipartimento di Ingegneria Navale, Elettrica, Elettronica e delle Telecomunicazioni, University of Genoa, 16154 Genova, Italy (e-mail: alberto.oliveri@unige.it).

Cinzia Beatrice, Enzo Ferrara, and Fausto Fiorillo are with the Istituto Nazionale di Ricerca Metrologica, 10135 Torino, Italy.

Color versions of one or more figures in this article are available at <https://doi.org/10.1109/TPEL.2024.3463803>.

Digital Object Identifier 10.1109/TPEL.2024.3463803

square-wave voltages are applied. The inductor is considered in these models as a conservative component, by modeling only the inductance as a nonlinear function of the current. Separate black-box loss models are provided, that depend on parameters (e.g., frequency, duty cycle, and bias current) specific to the application. These representations are therefore valid for the inductor within the specific dc–dc converter. Moreover, as losses are modeled separately, a unique circuit model is not available. Circuit models are instead proposed in [15], [16], and [17], composed of a nonlinear conservative inductor and some resistors accounting for the instantaneous losses. However, these models are validated at a single frequency and with a unique waveform only. Therefore, they are not sufficiently general to be used in circuit simulators for converter design and simulation purposes.

In the frequency range used in typical converter applications ( $f > 1$  kHz), the core losses are dominated by eddy currents. Many papers propose ladder circuit models, composed of inductors and resistors, to represent eddy currents, but only when the inductor works in its linear region [18], [19]. Fractional order models, which can be implemented as ladder circuits, are also very popular [20], [21]. Only a few attempts have been made to extend these models to the nonlinear operating region. In [22] and [23] a ladder circuit with nonlinear inductors is suggested for a wide frequency range, for application as a common mode choke within an inverter. The model is validated on a specific application (with a single waveform) but no simulation results showing measured and estimated currents or hysteresis loops at different frequencies and saturation levels are displayed.

Amorphous and nanocrystalline cores are a promising alternative to ferrite and iron-powder cores, for converter design [24], [25], [26], [27], [28], [29], [30], [31], [32] due to their extremely soft magnetic behavior and versatile response to annealing under saturating magnetic field [33]. They exhibit reduced magnetic losses up to very high frequencies, combined with low thickness, high electrical resistivity, and permeability, which depend weakly on temperature (in most cases almost linearly up to about 150 °C, due to their high Curie's temperature), unlike ferrites.

In this work, we propose a novel behavioral circuit model of amorphous-core inductors, with some temperature-dependent parameters, suitable for implementation in circuit simulators. The model is based on two coupled nonlinear inductors; this provides a clearer physical interpretation of the eddy currents. Unlike [22], [23], where measurements of magnetic fields  $B$  and  $H$  are used, the proposed model is identified based on inductor voltage and current measurements, easily obtainable also for commercial components, at different temperatures. The model permits one to reproduce the inductor behavior for different voltage waveforms (sinusoidal, square, and triangular), amplitudes (up to magnetic saturation), frequencies, current offsets, and temperatures. In addition, the average power loss is estimated with good accuracy. Unlike the models available in the literature, the proposed one is sufficiently general to allow for converter design and simulation in different operating conditions. The model is validated on two amorphous-core inductors with different characteristics, on a frequency range of 25–200 kHz, compatible with applications in power supplies. Moreover, the model is validated on a temperature range of 23 °C–100 °C. For



Fig. 1. Ribbons of  $\text{Co}_{67}\text{Fe}_4\text{B}_{14.5}\text{Si}_{14.5}$  (right) and  $\text{Co}_{71}\text{Fe}_4\text{B}_{15}\text{Si}_{10}$  (left) composing core 1 and 2, respectively.

TABLE I  
GEOMETRICAL AND PHYSICAL PROPERTIES OF CORE 1 AND 2

	Core 1	Core 2
Electrical resistivity ( $\Omega \text{ m}$ )	$141 \times 10^{-6}$	$124 \times 10^{-6}$
Mass (g)	0.3107	0.3249
Ribbon width (mm)	10	4.8
Cross-sectional area ( $\text{m}^2$ )	$7.80 \times 10^{-7}$	$7.37 \times 10^{-7}$
Thickness ( $\mu\text{m}$ )	11.5	16.93
Density ( $\text{kg}/\text{m}^3$ )	7730	7860
Saturation polarization (T)	0.5	0.89
Induced anisotropy ( $\text{J}/\text{m}^3$ )	7	240
Curie temperature ( $^{\circ}\text{C}$ )	310	385

comparison purposes, we also simulated a ladder circuit [22], [23] with a comparable number of parameters, and we show that our circuit shows better accuracy in modeling magnetic saturation.

The rest of this article is organized as follows. Section II analyzes the used magnetic cores and inductors. Section III describes the collected experimental measurements, whereas the proposed model is detailed in Section IV. The obtained results are shown in Section V. Finally, Section VI concludes this article.

## II. AMORPHOUS-CORE INDUCTORS

In this work, we consider two custom toroidal cores, referred to as *core 1* and *core 2*. They are made of rapidly solidified amorphous ribbons of composition  $\text{Co}_{67}\text{Fe}_4\text{B}_{14.5}\text{Si}_{14.5}$  and  $\text{Co}_{71}\text{Fe}_4\text{B}_{15}\text{Si}_{10}$ , respectively. The as-quenched ribbons (see Fig. 1) are tape wound as ring samples and encased in toroidal boron nitride holders (inside diameter 14 mm, outside diameter 20 mm), which are then subjected to thermal treatments under a saturating dc magnetic field, transverse to the ribbon width. The sequence of treatments, depending on the material composition, starts with stress-release annealing at a temperature  $T = 320$  °C – 360 °C, followed by cooling and prolonged stay at  $T = 280$  °C. Here, magnetic ordering by short-range atomic diffusion along the field direction takes place, resulting in a uniformly induced transverse anisotropy, a quantity that fully governs the magnetic response of the amorphous alloys. The main properties of the two cores are provided in Table I.

$B$ – $H$  hysteresis loops and core losses are measured under controlled sinusoidal waveform through a calibrated digital wattmeter (fluxmetric method) up to a few MHz and by a vector

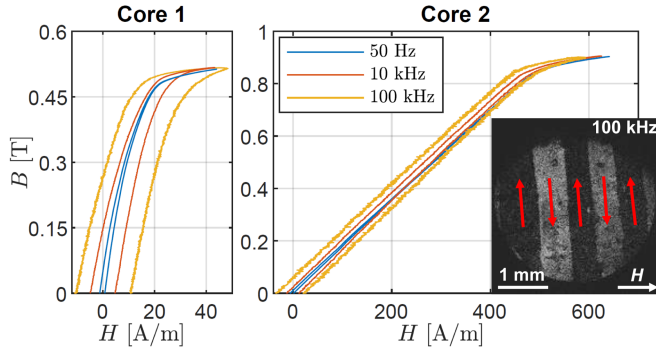


Fig. 2. Major hysteresis loops (for  $B \geq 0$  T) measured at three different frequencies (see legend) for core 1 (left) and 2 (right). The inset shows the domain structure at the coercive field, observed by the magneto-optical Kerr effect at 100 kHz in core 2. The magnetization inside the domains (red arrows) is transverse to the ribbon length and the applied ac field  $H$ .

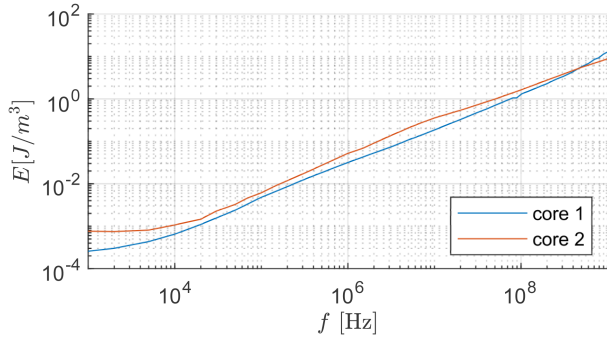


Fig. 3. Energy loss versus frequency measured in core 1 (blue curve) and 2 (orange curve), at a peak flux density value of 10 mT.

network analyzer from a few hundred kHz up to 1 GHz. Winding arrangements and electrical circuitry are set for minimum interference by the stray parameters [34].

The resulting major  $B$ – $H$  loops at 50 Hz (quasi-static condition, blue curves), 10 kHz (orange curves), and 100 kHz (yellow curves) are shown in Fig. 2 for core 1 (left) and 2 (right). The quasi-static loops show limited hysteresis and a quasi-linear magnetization curve, flattening on the approach to magnetic saturation. The magnetic losses are minimized because magnetic domains transverse to the ribbon length (i.e., the exciting field  $H$ ) are obtained by field annealing (see the magneto-optical inset in the figure) and the magnetization process chiefly occurs by spin rotations inside the domains [35]. The loop area, equal to the energy density  $E$  lost in a period, increases with the frequency  $f$ . This is shown in Fig. 3, where the measured  $E(f)$  behavior for peak magnetic induction  $B_p = 10$  mT is represented for both cores. Core 1 exhibits better loss performances up to about 400 MHz.

The very large difference in the required field strengths in core 1 and core 2 (see Fig. 2) is related to a correspondingly large difference in the induced anisotropies (see Table I). This effect descends from the specific field-annealing treatment adopted for the two cores and the inverse relationship existing between permeability and anisotropy energy.

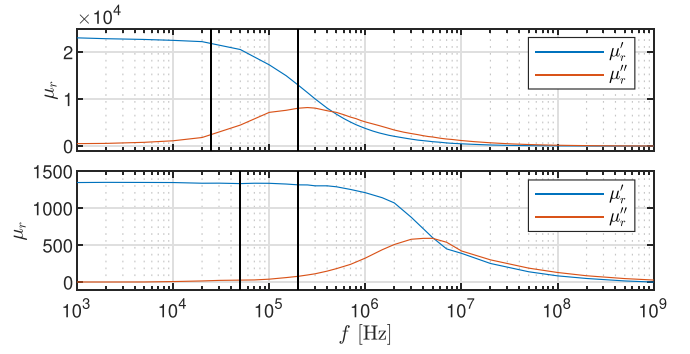


Fig. 4. Absolute value of real (blue) and imaginary (orange) permeability measured at peak flux density  $B_p = 10$  mT in core 1 (top panel) and 2 (bottom panel).

In soft magnetic cores, the total energy loss is considered as the sum of the hysteresis loss  $W_h$  (independent of frequency), the classical loss  $W_{cl}$  (increasing linearly with  $f$ ), and the excess loss  $W_{exc}$  (proportional to  $\sqrt{f}$ ). Eddy currents, generated in the metallic sample under time-dependent magnetization, are the chief source of dissipation in the amorphous ribbons. Localized parasitic eddies are responsible for the  $W_h$  and  $W_{exc}$  loss components, whereas  $W_{cl}$  descends from long-range eddy current patterns. With the transverse domain structure shown in Fig. 2,  $W_h$  and  $W_{exc}$  are minimized.

Fig. 4 provides an overview of the measured complex relative permeability

$$\mu_r = \mu_r' - j\mu_r'' \quad (1)$$

versus frequency in core 1 (top panel) and core 2 (bottom panel). The presence of an imaginary component  $\mu_r''$  indicates a phase shift between the sinusoidal fields  $H$  and  $B$ , i.e., energy loss. The frequency ranges considered in this work (described in the following sections) are delimited by black vertical lines. Notice that core 1 operates in a region where the complex permeability has a significant variation.

Two inductors (*inductor 1* and *inductor 2*) are created by winding a wire of thickness 0.2 mm around cores 1 and 2, with  $n = 20$  and  $n = 32$  turns, respectively. The current  $i$  flowing in the wire is proportional to the magnetic field  $H$ , and the flux  $\phi$  across the core section is proportional to the magnetic flux density  $B$ , namely,

$$i = \frac{\ell H}{n} \quad (2)$$

$$\phi = BA \quad (3)$$

where  $\ell$  and  $A$  denote the magnetic path length and the cross-sectional area of the core, respectively. The differential inductance can then be written as

$$L = n \frac{d\phi}{di} = \frac{n^2 A}{\ell} \frac{dB}{dH} = \frac{n^2 A}{\ell} \mu_0 (\mu_r' - j\mu_r'') \quad (4)$$

being  $\mu_0$  the vacuum permeability. By considering small-amplitude (so that the inductor can be assumed to be a linear



component) sinusoidal current  $i$  and voltage

$$v = n \frac{d\phi}{dt} \quad (5)$$

the inductor equation can be written in the phasor domain as

$$\hat{V} = j\omega L \hat{I} = \left[ \left( \frac{n^2 A \mu_0}{\ell} \omega \mu_r'' \right) + j\omega \left( \frac{n^2 A \mu_0}{\ell} \mu_r' \right) \right] \hat{I} \quad (6)$$

with  $\omega = 2\pi f$ . Consequently, the impedance of the inductor is

$$Z(j\omega) = \hat{R}(\omega) + j\omega \hat{L}(\omega) \quad (7)$$

being  $\hat{R}$  and  $\hat{L}$  proportional to  $\omega \mu_r''$  and  $\mu_r'$ , respectively.

### III. SETUP AND MEASUREMENTS

The amorphous alloys composing the inductor core have a weak temperature dependence of their properties (compared to ferrites). Indeed, for the majority of Co-based amorphous alloys (including those analyzed in this article), the maximum magnetic polarization (corresponding to magnetic saturation) decreases weakly and almost linearly with the temperature up to about 150 °C [36]. The parameters of the proposed circuit model are identified based on steady-state measurements of the inductor voltage  $v$  and current  $i$ . The electrical measurements are collected as explained in [16]. We performed three campaigns of measurements, providing three different datasets.

#### A. Dataset 1

For inductor 1, we impose sinusoidal, square, and triangular voltage waveforms (with duty cycle 50%) with eight fundamental frequencies (from 25 to 200 kHz, with a step of 25 kHz) and five amplitudes, so that the current amplitude ranges from about 0.02 A (amplitude #1) to 0.2 A (amplitude #5). For inductor 2, only sinusoidal and square waveforms are considered with frequency starting from 50 kHz and current ranging from 0.5 A (amplitude #1) to 1.3 A (amplitude #5). With sinusoidal voltage waveforms, a pure tone is imposed on the inductor. In contrast, square waves, endowed with a wide harmonic content, permit one to better identify and validate the behavior of the model with respect to frequency. Moreover, sinusoidal waveforms are applied, e.g., in inverters, whereas square-wave voltages are used in switching dc–dc converters. Triangular waves are imposed to further validate the model. The frequency ranges, imposed by the specifications of the adopted measuring circuit, are compatible with most power converter applications. All measurements are obtained at room temperature and the dc component of the currents is always zero.

A total of  $K_1$  time series  $\{\hat{v}^{(k)}(t), \hat{i}^{(k)}(t)\}$ , with  $k = 1, \dots, K_1$ , is then available for each inductor, where  $K_1 = 120$  for inductor 1 and 70 for inductor 2. These time series are filtered through a Savitzky-Golay smoothing filter (MATLAB function *sgolayfilt*), that is typically used to smooth out a noisy signal whose frequency span (without noise) is large, which is the case for the square waveforms. Here, an order 9 and frame length 35 are heuristically selected to remove the high-frequency noise without altering the signal. Fig. 5 shows the current resulting

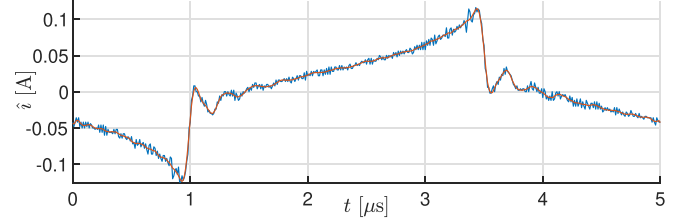


Fig. 5. Measured (blue curve) and filtered (orange curve) inductor 1 current, obtained by applying a square wave voltage with frequency 200 kHz and the largest amplitude.

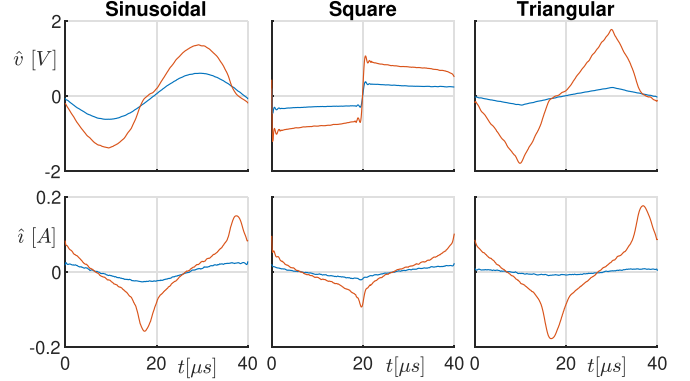


Fig. 6. Time evolution of inductor 1 voltage (top panels) and current (bottom panels), for sinusoidal (left), square (middle), and triangular waveforms at 25 kHz with amplitudes #1 (blue) and #5 (orange).

from the application of a 200 kHz square wave voltage before (blue curve) and after (orange) filtering.

For the  $k$ th time series, we define

$$\hat{\phi}^{(k)}(t) = \frac{1}{n} \int_0^t \hat{v}^{(k)}(\tau) d\tau. \quad (8)$$

The instantaneous and average power are evaluated as

$$\hat{p}^{(k)}(t) = \hat{v}^{(k)}(t) \hat{i}^{(k)}(t) \quad (9)$$

$$\langle \hat{p}^{(k)} \rangle = \frac{1}{\Delta T^{(k)}} \int_0^{\Delta T^{(k)}} \hat{p}^{(k)}(\tau) d\tau \quad (10)$$

respectively, where  $\Delta T^{(k)}$  is the period in the  $k$ th series.

Fig. 6 shows measurements of the inductor 1 voltage (top panels) and current (bottom panels) for sinusoidal (left), square (middle), and triangular wave (right) applied signals, at 25 kHz with amplitude #1 (blue curves) and #5 (orange curves). For small amplitude values, the inductor works in its linear region; as the amplitude increases the inductor approaches magnetic saturation, which causes evident distortions in the current. The distortions in the voltage are instead due to the shunt resistor and the nonzero output impedance of the power amplifier, employed in the measuring circuit [16].

Fig. 7 shows  $\hat{\phi}^{(k)}$  versus  $\hat{i}^{(k)}$  for inductor 1 with sinusoidal (left), square (middle), and triangular wave (right) applied signals at 50 kHz (top) and 200 kHz (bottom) for the amplitudes #1, #3, and #5.

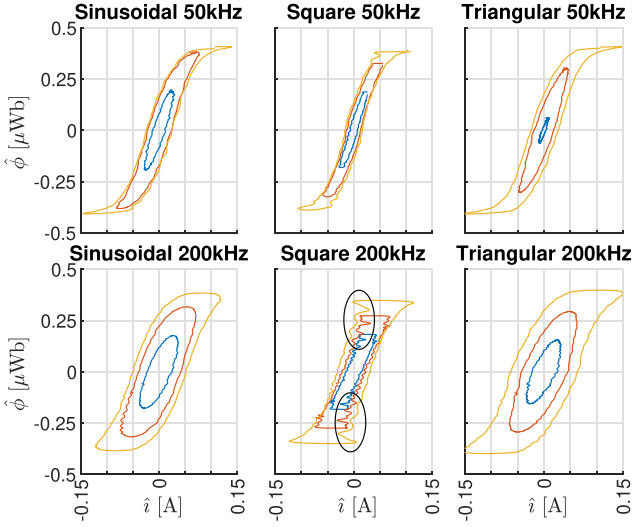


Fig. 7. Inductor 1: measured  $\phi$ - $i$  loops at 50 kHz (top panels) and 200 kHz (bottom panels), for sinusoidal (left), square (middle), and triangular (right) waveforms, with amplitudes #1 (blue), #3 (orange) and #5 (yellow).

The shape of the loop depends on the applied waveform, due to the dynamic nature of the magnetic losses. The loops obtained with sinusoidal waveforms are qualitatively similar to the ones shown in Fig. 2. The oscillations (highlighted with the black ellipses) obtained with high-frequency square voltages are caused by parasitic capacitances, as described in [37].

During these measurements, we did not experience any current drift due to a temperature increase, even when the inductor operates in saturation for a long time. Then, the temperature is not considered for these data. It is included in dataset 3.

### B. Dataset 2

This dataset is collected only on inductor 1 at room temperature and 25 kHz. We impose sinusoidal and square voltage waveforms (with duty cycle 50%) with five different dc components so that the mean current

$$\langle \hat{i}^{(k)} \rangle = \frac{1}{\Delta T^{(k)}} \int_0^{\Delta T^{(k)}} \hat{i}^{(k)}(\tau) d\tau \quad (11)$$

ranges from about 0 A to 45 mA. Moreover, we also impose square voltage waveforms with five different duty cycles, from 30% to 70% (with a step of 10%), thus obtaining currents with mean values from about -45 mA to 45 mA. A total of  $K_2 = 15$  time series is then available for this dataset, filtered as for dataset 1. With waveforms #2 and #3 the inductor current is a triangular wave (in the linear region) with an offset, which is the typical situation for inductors operating in switching dc-dc converters (e.g., buck, boost, or buck-boost converters).

### C. Dataset 3

We perform the measurements at three different temperatures (23 °C, 60 °C, and 100 °C). We impose sinusoidal waveforms with three amplitudes and three fundamental frequencies: 25, 50, and 100 kHz for inductor 1, 50, 100, and 200 kHz for inductor

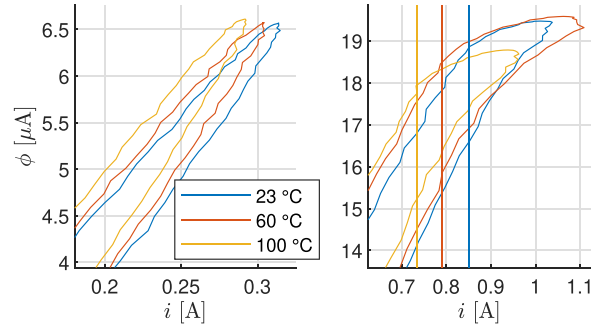


Fig. 8. Inductor 2: portions of measured loops at three different temperatures in the linear region (left panel) and up to saturation (right panel). Each vertical line (related to the loop with the same color) denotes the current value for which the effect of magnetic saturation starts to appear.

2. The measurements have been performed by placing the ring sample inside a cylindrical nylon holder (diameter 40 mm, height 45 mm), wrapped by a dc-supplied shielded heating element. The temperature was measured with a copper-constantan microthermocouple. The current offset is always 0. A total of  $K_3 = 27$  time series is then available for each inductor in this dataset, filtered as for the previous datasets. Fig. 8 shows measured flux-current loops on inductor 2 at 23 (blue), 60 (yellow), and 100 °C (orange). When the inductor operates in its linear region (left panel), the dependence on temperature is weak. On the contrary, as the temperature increases, magnetic saturation occurs for lower currents (right panel). This is a common behavior for amorphous alloys, but also ferrites and nanocrystalline materials. As shown in [36, Fig. 10] the value of the magnetic polarization  $J$  (related to  $B$ , being  $B = \mu_0 H + J$ ) in saturation decreases (almost linearly up to about 150 °C for amorphous cores similar to the ones used in this article) with  $T$  up to the Curie's temperature, where it vanishes.

## IV. INDUCTOR MODEL

### A. Proposed Model

If a time-varying current flows through the inductor winding, then a time-varying magnetic flux is generated in the core cross-section. As described in Section II, if the core is electrically conductive, a flux variation induces eddy currents inside the core, which generate, in turn, a counter field. In order to maintain a defined flux rate of change, the applied field must increase and the power loss is correspondingly enhanced. This phenomenon can be modeled through the circuit proposed in Fig. 9. The time-varying current  $i'_1$  generates a flux on inductor  $L_1$ , which, due to the magnetic coupling, induces a flux also on  $L_2$ . Being this flux time-varying, a voltage is applied to resistor  $R_2$  and then a current  $i'_2$  (related to the eddy currents) circulates in the right loop of the circuit. Resistors  $R_1$  and  $R_2$  model the ohmic losses due to thermal dissipation.  $R_{DC}$  is the dc resistance due to winding losses, whereas the series connection between  $R_C$  and  $C$  is inserted to model the parasitic capacitances leading to oscillations in the high-frequency square-wave measurements.

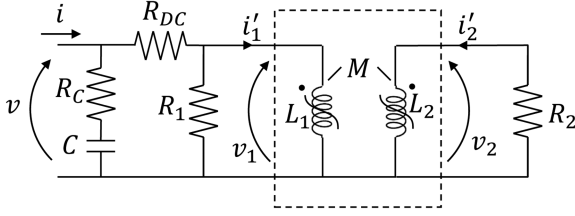


Fig. 9. Proposed circuit model, including the  $RC$  series (outside the dashed rectangle) to model the parasitic capacitances.

For constant temperature and low current values, far from the magnetic saturation, the inductances  $L_1$  and  $L_2$  are constant ( $L_1^0$  and  $L_2^0$ , respectively) and the inductor flux linkages<sup>1</sup> are as follows:

$$\begin{cases} \lambda_1 = L_1^0 i'_1 + M i'_2 = L_1^0 \left( i'_1 + \frac{M}{L_1^0} i'_2 \right) \\ \lambda_2 = M i'_1 + L_2^0 i'_2 = L_2^0 \left( \frac{M}{L_2^0} i'_1 + i'_2 \right) \end{cases} \quad (12)$$

where

$$M = \beta \sqrt{L_1^0 L_2^0} \quad (13)$$

with  $\beta \in [0, 1]$ , is the mutual inductance. If the coupling coefficient  $\beta = 0$ , then the inductors are completely uncoupled. On the contrary, if  $\beta = 1$ , the coupling is maximum. By defining

$$\eta \triangleq \sqrt{\frac{L_2^0}{L_1^0}} \quad (14)$$

$$i_1 \triangleq i'_1 + \beta \eta i'_2 \quad (15)$$

$$i_2 \triangleq \frac{\beta}{\eta} i'_1 + i'_2 \quad (16)$$

the coupled inductors equations can be recast as

$$\begin{cases} \lambda_1 = L_1^0 i_1 \\ \lambda_2 = L_2^0 i_2 \end{cases} \quad (17)$$

Currents  $i_1$  and  $i_2$ , resulting from the change of variables, also have a circuital meaning, as shown in Section IV-B.

Currents  $i'_1$ ,  $i'_2$  can be obtained from  $i_1$ ,  $i_2$ , by inverting (15) and (16)

$$\begin{cases} i'_1 = \frac{1}{1-\beta^2} i_1 - \frac{\beta \eta}{1-\beta^2} i_2 \\ i'_2 = \frac{1}{1-\beta^2} i_2 - \frac{\beta}{\eta(1-\beta^2)} i_1 \end{cases} \quad (18)$$

Voltages  $v_j$  ( $j = 1, 2$ ) can be expressed as

$$v_j = \frac{d\lambda_j}{dt} = \frac{d\lambda_j}{di_j} \frac{di_j}{dt} \quad (19)$$

where the differential inductances

$$L_j(i_j) = \frac{d\lambda_j}{di_j} \quad (20)$$

are equal to  $L_j^0$  in the linear region. The differential inductance can be assumed constant only when the inductor operates in

its linear region, otherwise, it has a strong dependence on the current. Many recent works [13], [39], [40] model the inductance as an arctangent function of the current, at a given temperature. Here, we exploit the same approach, by defining

$$L_j(i_j) = \alpha L_j^n + \frac{(1-\alpha)L_j^n}{\pi} \left\{ \frac{\pi}{2} - \arctan \left[ \sigma_j \left( \frac{|i_j|}{I_j} - 1 \right) \right] \right\} \quad (21)$$

where  $L_j^n$ ,  $\alpha$ ,  $\sigma_j$ , and  $I_j$  are parameters to be fitted to data. In particular,  $L_j^n$  controls the slope of the  $\lambda_j(i_j)$  characteristics for  $i_j \rightarrow 0$ ,  $\alpha L_j^n$  is the slope of the same curve for large values of  $i_j$  (magnetic saturation),  $I_j$  is related to the value of  $i_j$  such that the slope of the curve changes (i.e., magnetic saturation approaches), whereas  $\sigma_j$  controls the smoothness of the curve [40]. Given that  $L_j(0) = L_j^0$ , we obtain

$$L_j^n = \frac{2\pi L_j^0}{(\alpha+1)\pi + 2(1-\alpha)\arctan(\sigma_j)}. \quad (22)$$

By observing the measured loops shown in Fig. 8, we notice that (i) the slope of the loops for small current values (left panel) increases with  $T$ , and (ii) the value of  $i$  such that effects of magnetic saturation appear (vertical lines in the right panel) decreases with  $T$ . Moreover, the wire resistivity increases with  $T$ . Based on these aspects, and on previous works [39], [41], [42], we generalize the inductance model by introducing the dependence on temperature of some parameters. In particular, we impose

$$L_j^0 = \bar{L}_j^0 \left( 1 + \frac{T - T_0}{\tau_j^L} \right) \quad (23)$$

$$I_j = \bar{I}_j \left( 1 + \frac{T - T_0}{\tau_j^I} \right) \quad (24)$$

$$R_{DC} = \bar{R}_{DC} \left( 1 + \frac{T - T_0}{\tau^R} \right) \quad (25)$$

with  $T_0 = 23^\circ\text{C}$ . Here,  $\bar{L}_j^0$ ,  $\bar{I}_j$ , and  $\bar{R}_{DC}$  are the values of parameters  $L_j^0$ ,  $I_j$ , and  $R_{DC}$  at room temperature, whereas  $\tau_j^L$ ,  $\tau_j^I$ , and  $\tau^R$  are related to their rate of variation with  $T$ . With this choice, it turns out that the inductance  $L_j$  depends on both the current  $i_j$  and the temperature  $T$ . This implies that also parameter  $\eta$  [see (14)] depends on  $T$ . The above equations impose a linear dependence of the parameters on the temperature, which is of course valid in a limited range of  $T$ . By looking at [36, Fig. 10], it appears that the linearity range of Co-based alloys (VITROVAC 6030 and 6150) is from 0 to about  $150^\circ\text{C}$ . This is the typical temperature range in switching converter applications [43]. Our experimental setup is certified up to  $100^\circ\text{C}$ , therefore, we could not perform measurements at higher temperatures, however, for the above reasons we expect the proposed model to be valid at least up to  $150^\circ\text{C}$ . Henceforth, the dependence on  $T$  is omitted in the notation.

<sup>1</sup> The flux linkage  $\lambda$  is defined as the product between the magnetic flux through the core section and the number of turns, i.e.,  $\lambda = n\phi$  [38].

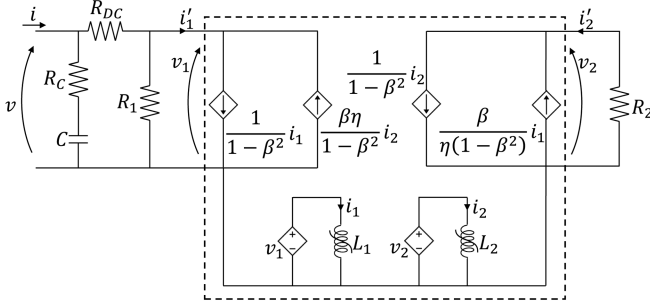


Fig. 10. Equivalent model suitable for circuit simulators.

The state equations of the circuit shown in Fig. 9 are as follows:

$$\begin{cases} L_1(i_1) \frac{di_1}{dt} = -\frac{R_p}{1-\beta^2} i_1 + \frac{\beta\eta R_p}{1-\beta^2} i_2 + \frac{R_p}{R_{DC}} v \\ L_2(i_2) \frac{di_2}{dt} = \frac{\beta R_2}{\eta(1-\beta^2)} i_1 - \frac{R_2}{1-\beta^2} i_2 \\ R_C C \frac{dv_c}{dt} = -v_c + v \end{cases} \quad (26)$$

with  $R_p = \frac{R_{DC} R_1}{R_{DC} + R_1}$ . Here,  $i_1$ ,  $i_2$ , and  $v_c$  are the state variables, whereas  $v$  is the input variable. The system output is the whole inductor current

$$i = \frac{(R_{DC} + R_1 + R_C)v - (R_{DC} + R_1)v_c + R_1 R_C i_1'}{R_C(R_{DC} + R_1)} \quad (27)$$

with  $i_1'$  given by the first (18).

The model depends on 18 parameters, collected in the vector  $\xi = [\bar{L}_1^0, \sigma_1, \bar{L}_1, \bar{L}_2^0, \sigma_2, \bar{L}_2, \alpha, \beta, \bar{R}_{DC}, R_1, R_2, R_C, C, \tau_1^L, \tau_1^I, \tau_2^L, \tau_2^I, \tau^R]$ , whose optimal value  $\xi^*$  can be obtained by solving the following nonlinear optimization problem:

$$\min_{\xi} \frac{1}{|\mathcal{K}|} \sum_{k \in \mathcal{K}} \mathcal{F}_k [i^{(k)}(t; \xi)] \quad (28)$$

where

$$\mathcal{F}_k [i(t)] = \sqrt{\frac{1}{\Delta T^{(k)}} \int_0^{\Delta T^{(k)}} [i(t) - \hat{i}^{(k)}(t)]^2 dt}. \quad (29)$$

Here,  $\mathcal{K}$  is the set of indices (with cardinality  $|\mathcal{K}|$ ) used for the parameter identification,  $\hat{i}^{(k)}(t)$  is the measured current in the  $k$ th time series, and  $i^{(k)}(t; \xi)$  is the current obtained by integrating system (26) with  $v(t) = \hat{v}^{(k)}(t)$ . The inductances and the other parameters depend on vector  $\xi$ .

### B. Equivalent Model Suitable for Circuit Simulators

Most circuit simulators (e.g., SPICE, PSIM, PLECS, Simscape) allow instantiating nonlinear inductors, by providing, e.g., the flux-current characteristics, but it may be difficult to implement nonlinear mutual inductors. However, (26) can also be implemented through the circuit shown in Fig. 10, relying on uncoupled nonlinear inductors, which is equivalent to the one shown in Fig. 9. In particular, the two-ports enclosed in the dashed rectangles in Figs. 9 and 10 have the same descriptive equations.

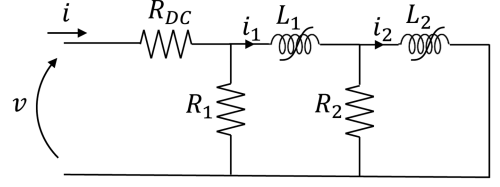


Fig. 11. Ladder circuit with two nonlinear inductors.

### C. Small-Signal Model

For very low-amplitude sinusoidal voltages and currents, we can assume that the inductors in Fig. 9 have constant inductances  $L_1^0$  and  $L_2^0$ . Therefore, we can compute the impedance of the physical inductor by considering the parallel connection between the  $RC$  series, with impedance  $\frac{1+j\omega R_C C}{j\omega C}$ , and the rest of the circuit in Fig. 9, whose impedance is  $\hat{R}'(\omega) + j\omega \hat{L}'(\omega)$ , with

$$\hat{R}'(\omega) = R_{DC} + \frac{\omega^2 R_1 [M^2 R_1 R_2 + (\omega\Delta)^2 + (L_1^0 R_2)^2]}{(R_1 R_2 - \omega^2 \Delta)^2 + \omega^2 \gamma^2} \quad (30)$$

$$\hat{L}'(\omega) = \frac{R_1^2 (L_1^0 R_2^2 + \omega^2 L_2^0 \Delta)}{(R_1 R_2 - \omega^2 \Delta)^2 + \omega^2 \gamma^2}, \quad (31)$$

$$\gamma = L_1^0 R_2 + L_2^0 R_1, \quad \Delta = L_1^0 L_2^0 - M^2. \quad (32)$$

The total impedance can be written as in (7).

### D. Benchmark Model

A ladder circuit with 6 nonlinear inductors is suggested in [22], [23], even if predictions of the inductor current for different frequencies and amplitudes are not provided. According to [23], each branch of the circuit models a portion of the core area. If the inductors are assumed to be linear components, our proposed model (excluding the  $RC$  series) has the same descriptive equations of the ladder circuit shown in Fig. 11, with 2 inductors, by assigning proper values to  $L_1$ ,  $L_2$ , and  $R_2$ . However, the equations become different if the inductances depend nonlinearly on the current. By applying Kirchhoff's laws and the descriptive equations of the components, we can derive the following state equations:

$$\begin{cases} L_1(i_1) \frac{di_1}{dt} = -(R_2 + R_p) i_1 + R_2 i_2 + \frac{R_p}{R_{DC}} v \\ L_2(i_2) \frac{di_2}{dt} = R_2 (i_1 - i_2) \end{cases} \quad (33)$$

with  $R_p = \frac{R_{DC} R_1}{R_{DC} + R_1}$  and the inductances modeled by (21). Here, currents  $i_1$  and  $i_2$  are the state variables, whereas  $v$  is the input voltage. The inductor current can be computed as

$$i = \frac{v + R_1 i_1}{R_{DC} + R_1}. \quad (34)$$

## V. RESULTS

In this section, we show the modeling results obtained with the three datasets described in Section III.



TABLE II  
OPTIMAL MODEL PARAMETERS FOR DATASET 1

	inductor 1	inductor 2
$\bar{L}_1^0$ [mH]	0.173	0.0271
$\sigma_1$	2.82	9.75
$\bar{I}_1$ [mA]	37.7	743
$\bar{L}_2^0$ [mH]	0.668	4.73
$\sigma_2$	1.88	19.4
$\bar{I}_2$ [mA]	15.1	1.60
$\alpha$	$6.2 \times 10^{-4}$	$13 \times 10^{-4}$
$\beta$	0.84	0.50
$\bar{R}_{DC}$ [ $\Omega$ ]	1.51	0.531
$R_1$ [ $\Omega$ ]	894	912
$R_2$ [ $\Omega$ ]	452	54.7
$R_C$ [ $\Omega$ ]	64.6	147
$C$ [nF]	0.962	12.5

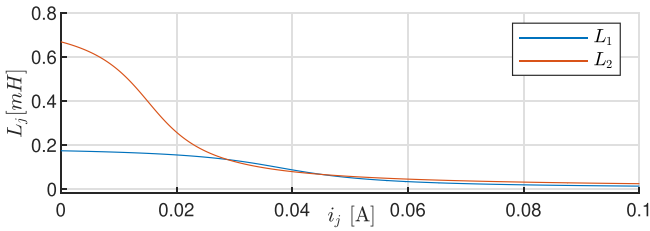


Fig. 12. Nonlinear inductances  $L_j(i_j)$  ( $j = 1, 2$ ) for inductor 1.

#### A. Dataset 1

Since all measurements in dataset 1 are obtained at  $T = T_0$ , the parameter vector  $\xi$  contains only the first 13 entries. Their optimal values are obtained by solving the optimization problem (28) in discrete time, with sampling times ranging from 10 ns (at 200 kHz) to 100 ns (at 25 kHz). A pattern search algorithm is used (MATLAB function *patternsearch*) starting from multiple random initial conditions. The set  $\mathcal{K}$  in problem (28) contains the indices of some measurements of dataset 1, i.e., those corresponding to sinusoidal and square-wave voltages with frequencies 25 kHz (50 kHz for inductor 2), 100 kHz (125 kHz for inductor 2), and 200 kHz, with the largest amplitude (#5); therefore, the cardinality of the set is  $|\mathcal{K}| = 6$ , meaning that only six time series are used to identify the model. The optimal parameters are listed in Table II for the two inductors, and the resulting nonlinear inductances  $L_j(i_j)$  ( $j = 1, 2$ ) are shown in Fig. 12 for inductor 1.

Simulations are performed by integrating (with the MATLAB function *ode45*) (26), with the optimal parameter vector  $\xi^*$  and  $v(t) = \hat{v}^{(k)}(t), \forall k$ , i.e., the voltage measurements in all available time series. The resulting estimated current is  $i^{(k)}(t; \xi^*)$ . The relative RMS error on the current is computed as

$$e_k = \frac{100}{i_{\max,k}} \mathcal{F}_k \left[ i^{(k)}(t; \xi^*) \right] \quad (35)$$

where  $i_{\max,k}$  is the maximum absolute value of the current in the  $k$ th time series. The error  $e_k$  is shown in color code in Fig. 13 for all considered time series for inductor 1 (a) and 2 (b). Here, the black rectangles mark the time series used to identify the model parameters. Some  $\phi$ - $i$  loops and time evolutions of the currents, corresponding to the capital letters in the figure, are shown in

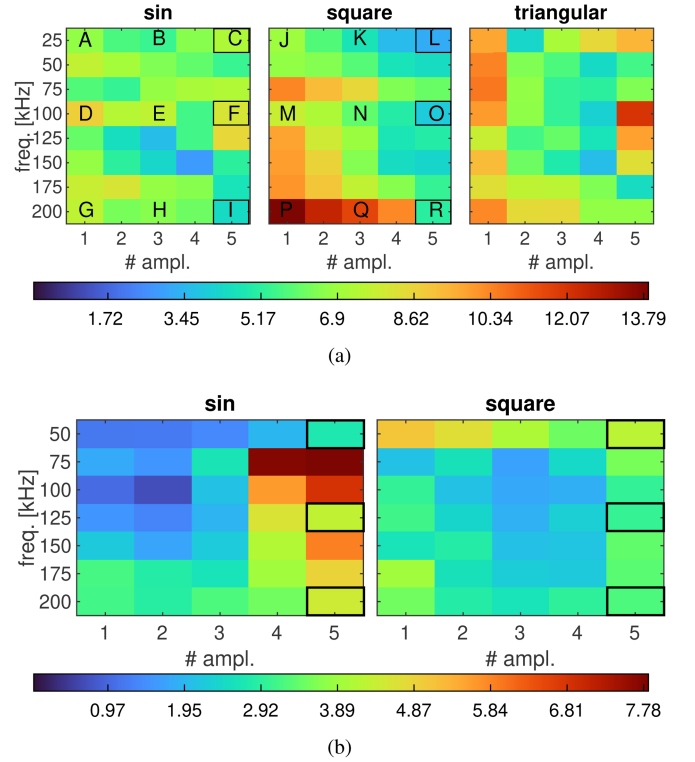


Fig. 13. Relative RMS error  $e_k$  for all considered time series for inductors 1 (a) and 2 (b). The black rectangles mark the time series used for model identification, whereas the capital letters correspond to the curves shown in Figs. 14 and 15.

Figs. 14 and 15, where the colored curves are the measurements, and the black dashed curves are the estimations. For inductor 1, in most cases the error is below 10%, even for the triangular waves, not used for model identification. Higher error values are obtained for amplitude #1 (square and triangular waves), where the measured current only reaches about 20 mA (see also Fig. 15) and the signal-to-noise ratio is lower. Fig. 16 shows that, owing to the  $RC$  series, the oscillations due to the parasitic capacitance of the winding are correctly predicted for amplitude #5 (time series R, top panel). The bottom panel shows the worst case (time series P), with  $e_k < 14\%$ .

For inductor 2, better performances are obtained, with  $e_k$  always below 8% (5% in most cases). This was expected since the complex permeability of the core does not change too much in the considered frequency range, as shown in Fig. 4.

Fig. 17 shows the measured (dots) and estimated (circles) average power losses for both inductors at all considered frequencies and amplitudes #1 (red), #3 (green), and #5 (blue). It is apparent that the proposed model can estimate the average power loss in all considered operating conditions, with a maximum absolute error of 27 mW for inductor 1 and 356 mW for inductor 2.

The small-signal model (see Section IV-C) is computed through  $\xi^*$  by considering the sinusoidal input with the smallest amplitude. The terms  $\hat{\frac{R}{\omega}}$  (related to  $\mu_r''$ , as described in Section II) and  $\hat{L}$  (related to  $\mu_r'$ ) are shown in Fig. 18 as solid orange and blue lines, respectively. The dots correspond to the

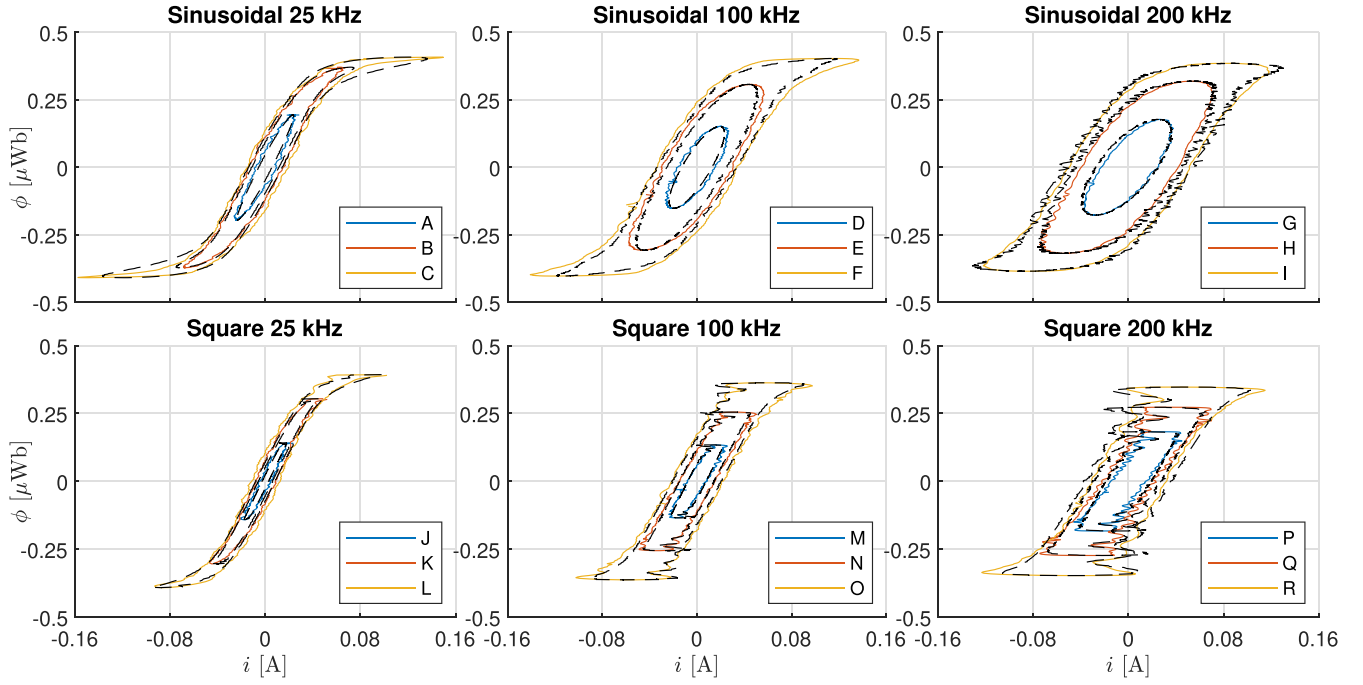


Fig. 14. Measured (colored curves) and estimated (dashed black curves)  $\phi$  versus  $i$  characteristics of inductor 1. The legends show the correspondence between the curves and the time series in Fig. 13.

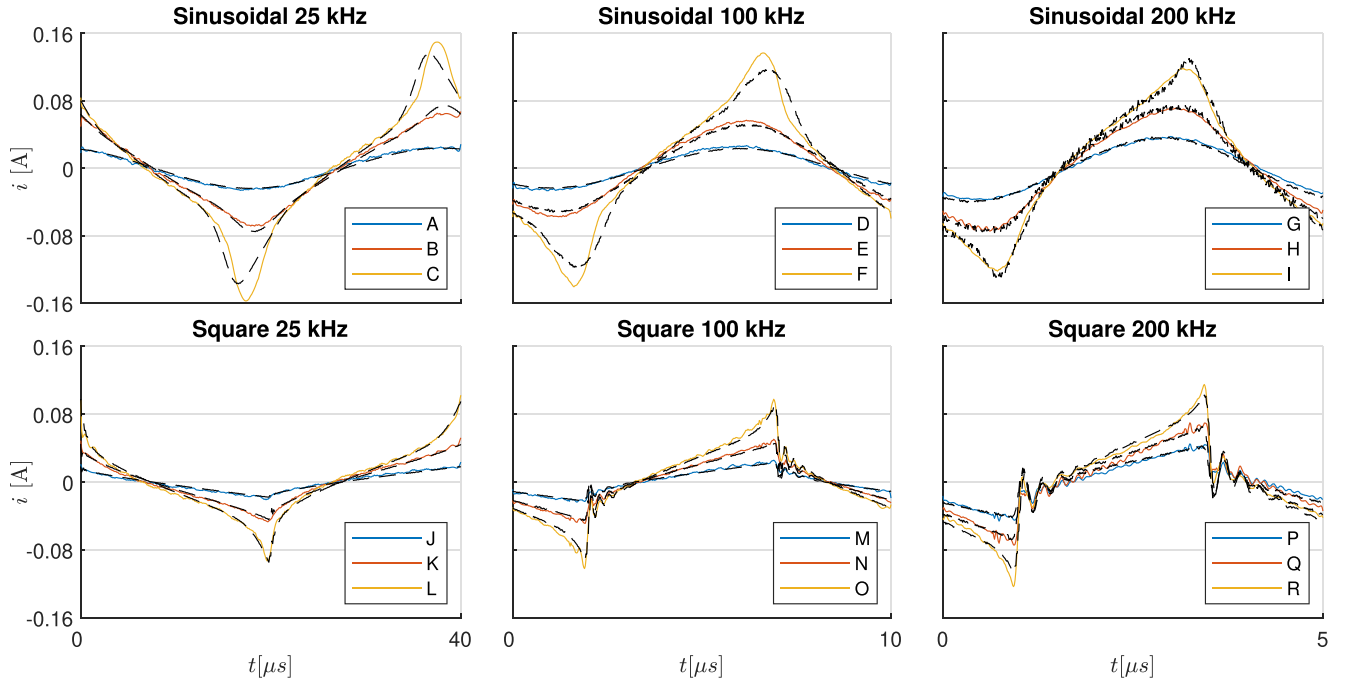


Fig. 15. Measured (colored curves) and estimated (dashed black curves) currents of inductor 1. The legends show the correspondence between the curves and the time series in Fig. 13.

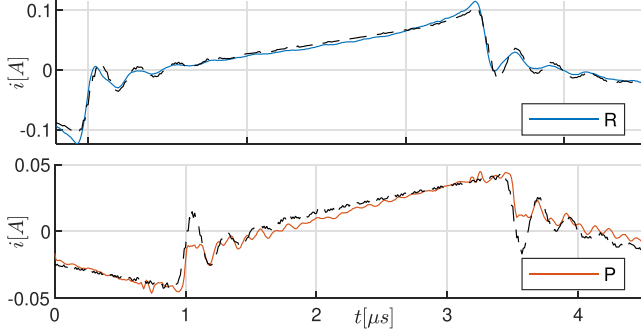


Fig. 16. Measured (colored curves) and estimated (dashed black curves) currents of inductor 1 in time series R (top) and P (bottom).

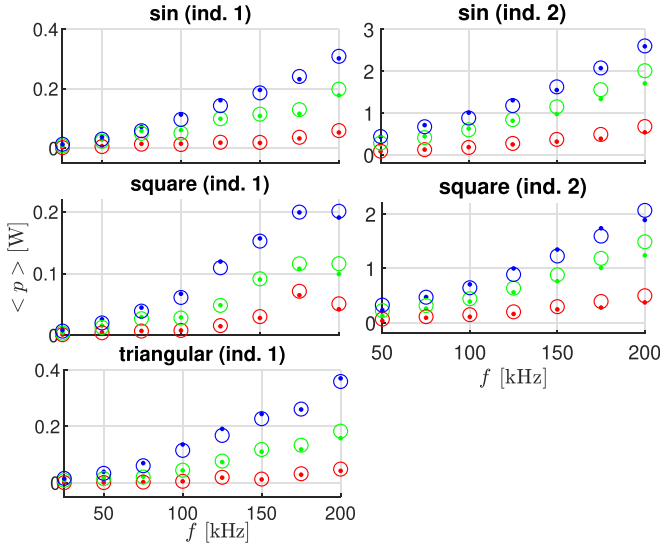


Fig. 17. Average power versus frequency for inductors 1 (left) and 2 (right). Amplitudes #1 (red), #3 (green), and #5 (blue).

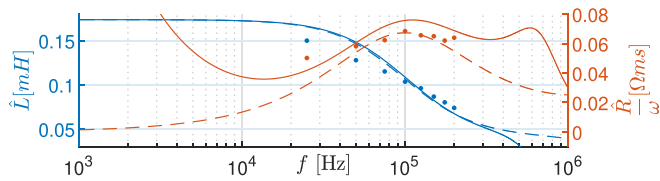


Fig. 18. Estimated resistance divided by  $\omega$  (orange lines) and inductance (blue lines) of the two-terminal element with  $R_{DC} = 0 \Omega$  and  $C = 0 \text{ F}$  (dashed lines) and of the complete two-terminal element (solid lines). The dots are the measured values.

measured inductance. Unlike the permeability plots of Fig. 4, the impedance  $Z(j\omega)$  [see (7), (30)–(32)] also considers the wire resistance  $R_{DC}$  – which influences the inductor behavior for low frequencies – and the winding parasitic capacitance, acting mainly at the high frequencies. For this reason the solid curves in Fig. 18 look different from the ones shown in Fig. 4. By contrast, if  $R_{DC}$  and  $C$  are set to 0, we obtain the dashed curves, which are similar to the curves shown in Fig. 4.

Finally, we compare our model to the benchmark model (see Fig. 11). We identified the parameters of the ladder model based

TABLE III  
OPTIMAL PARAMETERS OF THE LADDER MODEL FOR INDUCTOR 1

parameter	value
$L_1^0$	0.012 mH
$\sigma_1$	3.01
$I_1$	25.7 mA
$L_2^0$	0.170 mH
$\sigma_2$	2.88
$I_2$	36.3 mA
$\alpha$	$1 \times 10^{-3}$
$R_{DC}$	1.43 $\Omega$
$R_1$	525 $\Omega$
$R_2$	191 $\Omega$

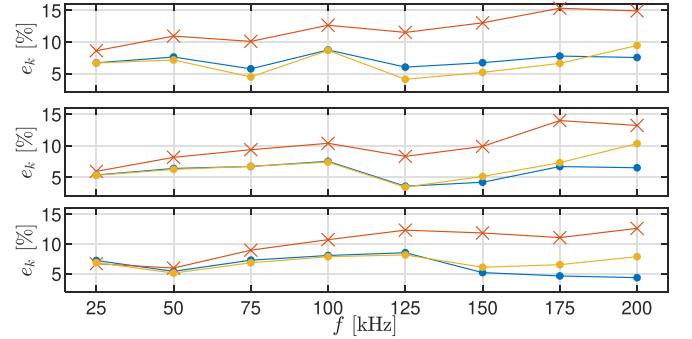


Fig. 19. Relative RMS error  $e_k$  obtained with the proposed model (blue curves), the proposed model with  $C = 0$  (yellow), and the ladder model (orange) for the sinusoidal waveforms with all frequencies and amplitudes #1 (top panel), #3 (middle), and #5 (bottom).

only on sinusoidal voltages at all frequencies and with the largest amplitude, for inductor 1. The optimal model parameters are shown in Table III. Fig. 19 shows the error  $e_k$  for all frequencies and amplitudes #1 (top panel), #3 (middle), and #5 (bottom) with the proposed model (blue curves), the same model without the RC branch (yellow curves), and the ladder model (orange curves). The yellow curves are shown to enable a fairer comparison between the benchmark model (where the RC branch is absent) and the proposed model. The error obtained with the ladder model is systematically higher than the one obtained with the proposed model.

## B. Dataset 2

As in dc–dc converters is common that the inductor operates with a relatively high dc bias and with duty cycles other than 50 %, we validate both the proposed model (see Table II) and the ladder model (see Table III) on the measurements in dataset 2. Fig. 20 shows all measured (colored curves) and estimated currents (black dashed curves) obtained with the proposed model, for dataset 2. Fig. 21 shows the error  $e_k$  as a function of the mean current, for sine waves with dc bias (blue), square waves with dc bias and duty cycle 50 % (orange), and square waves with duty cycle ranging from 30 to 70 % (yellow). The errors obtained with the proposed model are always below 10 %.

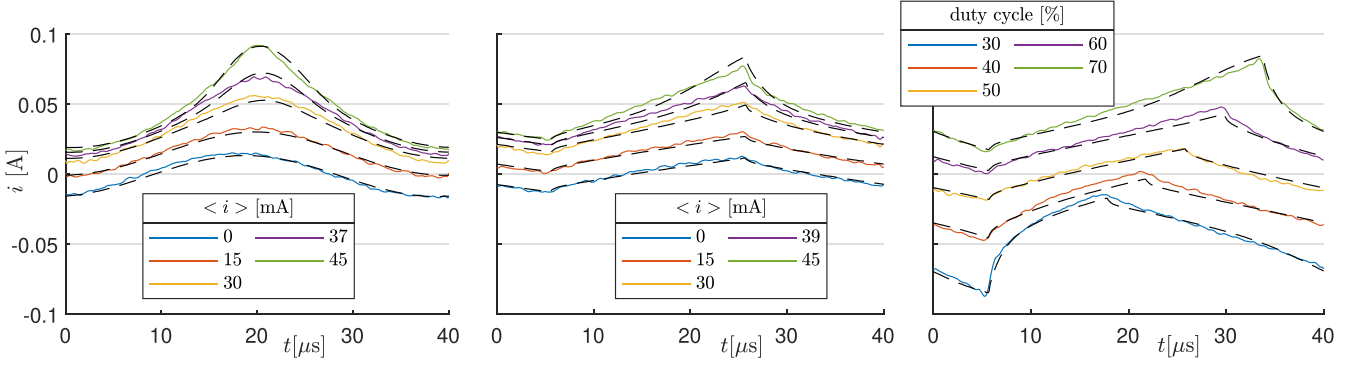


Fig. 20. Measured (colored curves) and estimated (dashed black curves) currents with a DC offset for inductor 1.

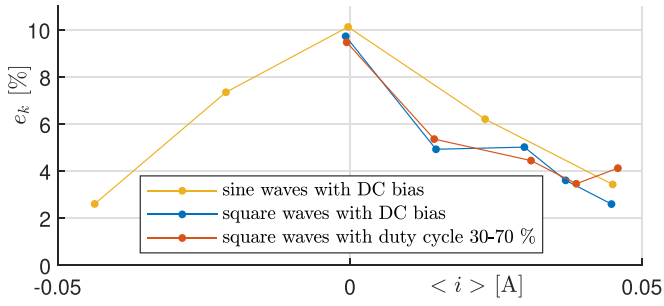


Fig. 21. Error  $e_k$  as a function of the mean current, for waveforms #1 (blue), #2 (orange), and #3 (yellow).

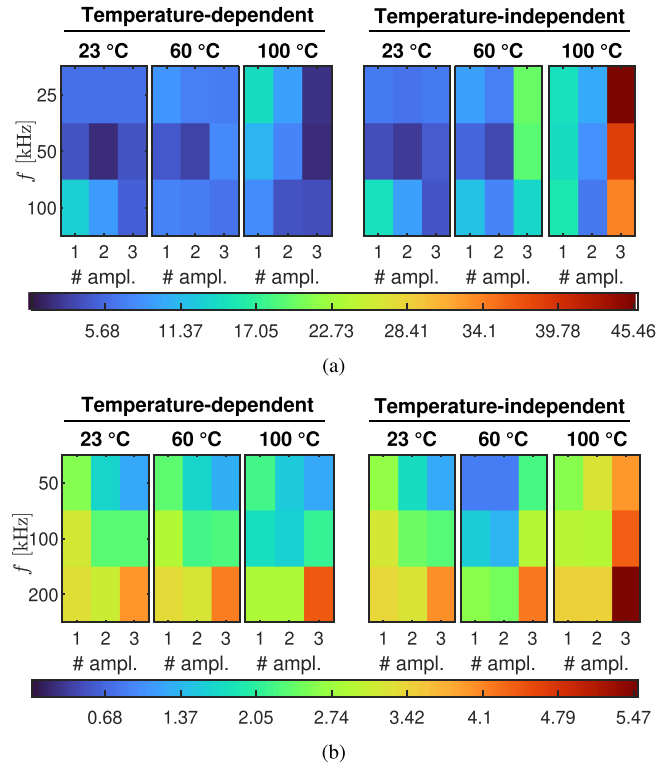


Fig. 22. Relative RMS error  $e_k$  for all considered time series for inductors 1 (a) and 2 (b), obtained by using the proposed model in its complete (temperature-dependent) version (left side) and in its temperature-independent version (right side).

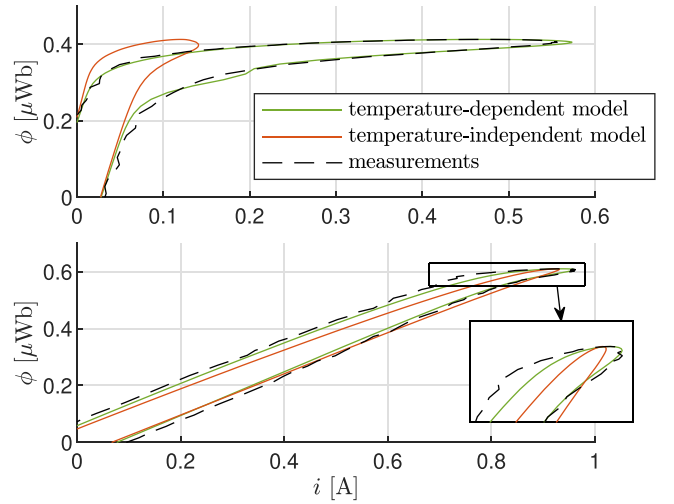


Fig. 23. Flux-current loops obtained at  $T = 100^\circ\text{C}$  for inductor 1 (top panel, 50 kHz) and 2 (bottom panel, 100 kHz). Measurements: black curves; estimation with temperature-dependent model: green curves; estimation with temperature-independent model: orange curves.

### C. Dataset 3

Finally, we want to test the complete model, by including also the dependence on the temperature, which can be significantly higher than  $23^\circ\text{C}$  in some circuits. To this end, the complete model (with 18 parameters) has been fitted to data in dataset 3, thus identifying from scratch vector  $\xi^*$  by solving the optimization problem (28). Set  $\mathcal{K}$  in (28) contains the indices of the measurements of dataset 3 corresponding to voltages with temperatures 23, 60, and  $100^\circ\text{C}$ , frequencies 25 kHz (50 kHz for inductor 2), and 100 kHz (200 kHz for inductor 2), with the largest amplitude. Then, the cardinality of the set is  $|\mathcal{K}| = 6$ . The optimal parameters are listed in Table IV for the two inductors. The dc resistance and the inductances at 0 current ( $L_1^0, L_2^0$ ) grow as  $T$  increases, whereas the currents  $I_1^0$  and  $I_2^0$  decrease. The relative RMS error  $e_k$  on all the time series in dataset 3 is shown in the left side of Fig. 22 for inductor 1 (a) and inductor 2 (b). The errors are below 14% (4.5%) for inductor 1 (2), for all considered measurements. The right side of Fig. 22 shows the error obtained without considering the dependence on



TABLE IV  
OPTIMAL MODEL PARAMETERS FOR DATASET 3

	inductor 1	inductor 2
$\bar{L}_1^0$ [mH]	0.180	0.0270
$\sigma_1$	2.82	9.25
$\bar{I}_1$ [mA]	37.7	750
$\bar{L}_2^0$ [mH]	0.705	5.20
$\sigma_2$	1.88	20.94
$\bar{I}_2$ [mA]	18.8	2.60
$\alpha$	$6.2 \times 10^{-4}$	$16 \times 10^{-4}$
$\beta$	0.85	0.43
$\bar{R}_{DC}$ [ $\Omega$ ]	0.25	0.7
$R_1$ [ $\Omega$ ]	800	838
$R_2$ [ $\Omega$ ]	451	54.8
$R_C$ [ $\Omega$ ]	64.6	147
$C$ [nF]	0.962	12.5
$\tau_1^L$ [ $^\circ\text{C}$ ]	$1.30 \times 10^3$	$6.64 \times 10^3$
$\tau_1^I$ [ $^\circ\text{C}$ ]	-750	-377
$\tau_2^L$ [ $^\circ\text{C}$ ]	$2.65 \times 10^5$	$1.67 \times 10^4$
$\tau_2^I$ [ $^\circ\text{C}$ ]	-26	-503
$\tau^R$ [ $^\circ\text{C}$ ]	218	88.7

temperature, i.e., by setting  $L_j^0 = \bar{L}_j^0$ ,  $I_j = \bar{I}_j$  ( $j = 1, 2$ ), and  $R_{DC} = \bar{R}_{DC}$  [see (23)–(25)] and using only 13 parameters. In this case, as  $T$  increases, also the error grows, especially for inductor 1, where it reaches about 45 % at  $100^\circ\text{C}$ . This suggests that for components working at temperatures significantly higher than  $23^\circ\text{C}$  the temperature dependence cannot be neglected.

Fig. 23 shows the measured (black) and estimated (green) flux-current loop obtained at  $100^\circ\text{C}$  for inductor 1 at 50 kHz (top panel) and inductor 2 at 100 kHz (bottom panel). The orange loops are the ones obtained without including the dependence on  $T$ . It is apparent that the temperature-dependent model fits better the measurements in the saturation region, especially for inductor 1.

## VI. CONCLUSION

A nonlinear circuit model of amorphous-core inductors is proposed that allows one to reproduce the inductor current and losses in different operating conditions (waveform, frequency, amplitude of the applied voltage, current dc offset, and temperature) by obtaining better results compared to already available ladder circuits. A few time series of voltage and current measurements are sufficient to identify the model parameters. The proposed model can be easily embedded in power converter circuit models, for the optimal design and simulation of converters exploiting inductors working up to magnetic saturation. This could lead to obtaining higher power density, by reducing the weight and size of magnetic components. At constant temperatures, we expect that the proposed model can reproduce the behavior of ferrite-, amorphous-, and nanocrystalline-core inductors, being characterized by qualitative similar magnetic behaviors. By contrast, if the temperature variation is included, the model can be applied to amorphous- and nanocrystalline-core inductors up to  $150^\circ\text{C}$  if their Curie's temperature is above  $300^\circ\text{C}$ , as a rule of thumb. Ferrites have instead a stronger and more complex dependence on temperature, in particular, their losses have a nonmonotonic dependence on  $T$  [44]. Then, a more accurate

model is probably necessary, even for lower temperatures, based on the curves shown in the material datasheets [10], [45], [46].

## REFERENCES

- [1] L. Milner and G. A. Rincón-Mora, "Small saturating inductors for more compact switching power supplies," *IEEJ Trans. Elect. Electron. Eng.*, vol. 7, no. 1, pp. 69–73, 2012.
- [2] G. Di Capua, N. Femia, and K. Stoyka, "Switching power supplies with ferrite inductors in sustainable saturation operation," *Int. J. Elect. Power Energy Syst.*, vol. 93, pp. 494–505, 2017.
- [3] N. Femia, K. Stoyka, and G. Di Capua, "Impact of inductors saturation on peak-current mode control operation," *IEEE Trans. Power Electron.*, vol. 35, no. 10, pp. 10969–10981, Oct. 2020.
- [4] M. S. Perdigão, J. P. F. Trovão, J. M. Alonso, and E. S. Saraiva, "Large-signal characterization of power inductors in EV bidirectional DC–DC converters focused on core size optimization," *IEEE Trans. Ind. Electron.*, vol. 62, no. 5, pp. 3042–3051, May 2015.
- [5] Z. Yao et al., "Nonlinear inductor-based single sensor current balancing method for interleaved DC–DC converters," *IEEE Trans. Power Electron.*, vol. 39, no. 4, pp. 3996–4000, Apr. 2024.
- [6] W. Yuan, Y. Wang, D. Liu, F. Deng, and Z. Chen, "Impacts of inductor nonlinear characteristic in multiconverter microgrids: Modeling, analysis, and mitigation," *IEEE J. Emerg. Sel. Top. Power Electron.*, vol. 8, no. 4, pp. 3333–3347, Dec. 2020.
- [7] Z. Özkan and A. M. Hava, "Current control of single-phase VSC systems with inductor saturation using inverse dynamic model-based compensation," *IEEE Trans. Ind. Electron.*, vol. 66, no. 12, pp. 9268–9277, Dec. 2019.
- [8] Z. Özkan and A. M. Hava, "Inductor saturation compensation in three-phase three-wire voltage-source converters via inverse system dynamics," *IEEE Trans. Ind. Electron.*, vol. 69, no. 5, pp. 4309–4319, May 2022.
- [9] J. Kaiser and T. Dürbaum, "An overview of saturable inductors: Applications to power supplies," *IEEE Trans. Power Electron.*, vol. 36, no. 9, pp. 10766–10775, Sep. 2021.
- [10] Magnetics, "Ferrite cores catalog," Accessed: Aug. 7, 2024. [Online]. Available: <https://www.mag-inc.com/Media/Magnetics/File-Library/Product%20Literature/Ferrite%20Literature/Magnetics-2021-Ferrite-Catalog.pdf>
- [11] R. A. Salas, J. Pleite, E. Olias, and A. Barrado, "Nonlinear saturation modeling of magnetic components with an RM-type core," *IEEE Trans. Magn.*, vol. 44, no. 7, pp. 1891–1893, Jul. 2008.
- [12] H. Chen, Z. Qian, S. Yang, and C. Wolf, "Finite-element modeling of saturation effect excited by differential-mode current in a common-mode choke," *IEEE Trans. Power Electron.*, vol. 24, no. 3, pp. 873–877, Mar. 2009.
- [13] A. Oliveri, M. Lodi, and M. Storace, "Nonlinear models of power inductors: A survey," *Int. J. Circuit Theory Appl.*, vol. 50, no. 1, pp. 2–34, 2022.
- [14] D. Scirè, G. Lullo, and G. Vitale, "Non-linear inductor models comparison for switched-mode power supplies applications," *Electronics*, vol. 11, no. 15, 2022, Art. no. 2472.
- [15] A. Oliveri, M. Lodi, C. Beatrice, E. Ferrara, M. Storace, and F. Fiorillo, "Behavioral model of an amorphous-core inductor working up to partial saturation," in *Proc. - IEEE Int. Symp. Circuit Syst.*, Austin, TX, USA, May, 2022, pp. 1522–1526.
- [16] A. Ravera, A. Oliveri, M. Lodi, and M. Storace, "A nonlinear behavioral model of a ferrite-core inductor with fixed-frequency sinusoidal voltage input," in *Proc. - IEEE Int. Conf. Smart Technol.*, Torino, Italy, Jul. 2023, pp. 418–422.
- [17] A. Ravera, A. Formentini, M. Lodi, A. Oliveri, M. Passalacqua, and M. Storace, "Modeling the effect of air-gap length and number of turns on ferrite-core inductors working up to magnetic saturation in a buck converter," *IEEE Trans. Circuit Syst. I*, early access, Jul. 11, 2024, doi: [10.1109/TCSI.2024.3421261](https://doi.org/10.1109/TCSI.2024.3421261).
- [18] X. Liu et al., "Behavioral modeling of complex magnetic permeability with high-order debye model and equivalent circuits," *IEEE Trans. Electromagn. Compat.*, vol. 63, no. 3, pp. 730–738, Jun. 2021.
- [19] D. Deswal and F. De León, "Generalized circuit model for eddy current effects in multi-winding transformers," *IEEE Trans. Power Deliv.*, vol. 34, no. 2, pp. 638–650, Apr. 2019.
- [20] N. Mijat, D. Jurisic, and G. S. Moschytz, "Analog modeling of fractional-order elements: A classical circuit theory approach," *IEEE Access*, vol. 9, pp. 110309–110331, 2021.

- [21] L. Zhang, A. Kartci, A. Elwakil, H. Bagci, and K. N. Salama, "Fractional-order inductor: Design, simulation, and implementation," *IEEE Access*, vol. 9, pp. 73695–73702, 2021.
- [22] B. Wunsch, S. Skibin, V. Forsstrom, and T. Christen, "Broadband modeling of magnetic components with saturation and hysteresis for circuit simulations of power converters," *IEEE Trans. Magn.*, vol. 54, no. 11, 2018, Art. no. 7301505.
- [23] C. R. Sullivan and A. Muetze, "Simulation model of common-mode chokes for high-power applications," *IEEE Trans. Ind. Appl.*, vol. 46, no. 2, pp. 884–891, Mar./Apr. 2010.
- [24] G. Herzer, "Nanocrystalline soft magnetic alloys," in *Handbook of Magnetic Materials*. New York, NY, USA: Elsevier, 1997, vol. 10, pp. 415–462.
- [25] P. Deck and C. P. Dick, "Power electronic building-block using an inverse coupled inductor based on tape-wound cores," in *Proc. - IEEE Int. Energy Sustain. Conf.*, Cologne, Germany, Jun. 2016, pp. 1–6.
- [26] J. Petzold, "Applications of nanocrystalline softmagnetic materials for modern electronic devices," *Scr. Mater.*, vol. 48, no. 7, pp. 895–901, 2003.
- [27] K. Praveena, K. Sadhana, S. Bharadwaj, and S. Murthy, "Development of nanocrystalline Mn–Zn ferrites for forward type DC–DC converter for switching mode power supplies," *Mater. Sci. Eng. Energy Syst.*, vol. 5, no. 1, pp. 56–61, 2010.
- [28] R. Hasegawa, "Applications of amorphous magnetic alloys in electronic devices," *J. Non-Cryst. Solids*, vol. 287, no. 1–3, pp. 405–412, 2001.
- [29] D. Ruiz-Robles, J. Ortíz-Marín, V. Venegas-Rebollar, E. L. Moreno-Goytia, D. Granados-Lieberman, and J. R. Rodríguez-Rodríguez, "Nanocrystalline and silicon steel medium-frequency transformers applied to DC–DC converters: Analysis and experimental comparison," *Energies*, vol. 12, no. 11, 2019, Art. no. 2062.
- [30] B. Tiwari, P. G. Bahubalindruni, J. Goes, and P. Barquinha, "Positive-negative DC–DC converter using amorphous–InGaZnO TFTs," *Int. J. Circuit Theory Appl.*, vol. 48, no. 3, pp. 394–405, 2020.
- [31] J. Ji and Z. Zhao, "Hysteresis characteristics prediction method of nanocrystalline and amorphous strips considering skin effect and non-sinusoidal excitation," *IEEE Trans. Power Electron.*, vol. 39, no. 4, pp. 3891–3905, 2024.
- [32] Y. Li, Z. Luo, Y. Li, J. Zhu, and B. Zhang, "Modelling of Fe-based soft magnetic materials for multi-physical analysis of medium frequency transformers," *IEEE Trans. Power Electron.*, vol. 39, no. 10, pp. 12249–12260, Oct. 2024.
- [33] R. Hasegawa, "Present status of amorphous soft magnetic alloys," *J. Magn. Magn. Mater.*, vol. 215, pp. 240–245, 2000.
- [34] F. Fiorillo, *Measurement and Characterization of Magnetic Materials*. San Diego, CA, USA: Academic Press-Elsevier, 2004.
- [35] C. Beatrice et al., "Broadband magnetic losses of nanocrystalline ribbons and powder cores," *J. Magnetism Magn. Mater.*, vol. 420, pp. 317–323, 2016.
- [36] Vacuumschmelze, "Soft magnetic materials and semi-finished products," Accessed: Aug. 7, 2024. [Online]. Available: [https://vacuumschmelze.com/03\\_Documents/Brochures/PHT%20001%20en.pdf](https://vacuumschmelze.com/03_Documents/Brochures/PHT%20001%20en.pdf)
- [37] D. Serrano et al., "Why MagNet: Quantifying the complexity of modeling power magnetic material characteristics," *IEEE Trans. Power Electron.*, vol. 38, no. 11, pp. 14292–14316, Nov. 2023.
- [38] W. G. Hurley and W. H. Wölfe, *Transformers and Inductors for Power Electronics: Theory, Design and Applications*. Hoboken, NJ, USA: Wiley, 2013.
- [39] G. D. Capua and N. Femia, "A novel method to predict the real operation of ferrite inductors with moderate saturation in switching power supply applications," *IEEE Trans. Power Electron.*, vol. 31, no. 3, pp. 2456–2464, Mar. 2016.
- [40] A. Oliveri, G. Di Capua, K. Stoyka, M. Lodi, M. Storace, and N. Femia, "A power-loss-dependent inductance model for ferrite-core power inductors in switch-mode power supplies," *IEEE Trans. Circuit Syst. I*, vol. 66, no. 6, pp. 2394–2402, Jun. 2019.
- [41] F. Bizzarri, M. Lodi, A. Oliveri, A. Brambilla, and M. Storace, "A nonlinear inductance model able to reproduce thermal transient in SMPS simulations," in *Proc. - IEEE Int. Symp. Circuit Syst.*, Sapporo, Japan, May 2019, pp. 1–5.
- [42] G. Vitale, G. Lullo, and D. Scirè, "Thermal stability of a DC/DC converter with inductor in partial saturation," *IEEE Trans. Ind. Electron.*, vol. 68, no. 9, pp. 7985–7995, Sep. 2021.
- [43] Y. Xiao, Z. Zhang, M. S. Duraij, T.-G. Zsurzsan, and M. A. Andersen, "Review of high-temperature power electronics converters," *IEEE Trans. Power Electron.*, vol. 37, no. 12, pp. 14831–14849, Dec. 2022.
- [44] F. Fiorillo et al., "Soft magnetic materials," in *Wiley Encyclopedia of Electrical and Electronics Engineering*. Hoboken, NJ, USA: Wiley, 2016, pp. 1–42.
- [45] TDK, "Mn-zn ferrite," Accessed: Aug. 7, 2024. [Online]. Available: [https://product.tdk.com/system/files/dam/doc/product/ferrite/ferrite/ferrite-core/catalog/ferrite\\_mn-zn\\_material\\_characteristics\\_en.pdf](https://product.tdk.com/system/files/dam/doc/product/ferrite/ferrite/ferrite-core/catalog/ferrite_mn-zn_material_characteristics_en.pdf)
- [46] TDG, "Soft ferrite materials," Accessed: Aug. 7, 2024. [Online]. Available: [https://product.tdk.com/system/files/dam/doc/product/ferrite/ferrite/ferrite-core/catalog/ferrite\\_mn-zn\\_material\\_characteristics\\_en.pdf](https://product.tdk.com/system/files/dam/doc/product/ferrite/ferrite/ferrite-core/catalog/ferrite_mn-zn_material_characteristics_en.pdf)



**Alessandro Ravera** (Student Member, IEEE) received the B.Sc. degree in electronic engineering and information technology and the M.Sc. degree in electronic engineering both from the University of Genoa, Genoa, Italy, in 2019 and 2021, respectively. He has been working toward the Ph.D. degree in electrical engineering with the University of Genoa, since November 2021.

His current research interests are in the modeling of nonlinear systems and the design and implementation of digital embedded systems.



**Alberto Oliveri** (Member, IEEE) received the M.Sc. degree in electronic engineering and the Ph.D. degree in electrical engineering both from the University of Genoa (UNIGE), Genoa, Italy, in 2009 and 2013, respectively.

He is currently an Associate Professor with the Department of Electrical, Electronic, Telecommunications Engineering, and Naval Architecture, (UNIGE). His main research interests include nonlinear modeling (applied to power electronics, power grids, and soft robotics) and predictive control.



**Matteo Lodi** (Member, IEEE) received the Laurea (M.Sc.) degree in electronic engineering and the Ph.D. degree in electrical engineering from the University of Genoa, Genoa, Italy, in 2015 and 2019, respectively.

He currently holds a postdoctoral position with the Department of Electrical, Electronic, Telecommunications Engineering, and Naval Architecture, University of Genoa. His main research interests are in the area of modeling of nonlinear systems, bifurcation analysis, and nonlinear dynamics.



**Cinzia Beatrice**, born in Torino, Italy, in 1958. She received the Laurea degree in physics from the University of Modena, Modena, Italy, in 1982, and the Ph.D. degree in physics from Politecnico di Torino, Torino, Italy, in 1987.

She has been a Research Scientist with the IEN Galileo Ferraris in Torino, since 1987. Currently, she holds the position of Senior Researcher since 1997 at INRIM. From 1995 to 2002, she was Responsible for Training and Diffusion of Scientific Culture. Her research activity has covered many aspects of the

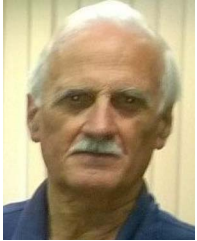
magnetization process in soft and permanent magnetic material, as hysteresis, energy losses, complex permeability and thermal relaxation effects.

Dr. Beatrice organized SMM11 (1993), SMM19 (2009), 2-DM (1993), she was Chair of the Organizing Committee for 2-DM 2014 in Torino, she was Co-chair of AIM2023 (Advances in Magnetism) IEEE International Conference in Moena. She is co-author of some 130 scientific papers and 6 technical reports.



**Enzo Ferrara** received the Laurea degree in chemistry from the University of Turin (Italy), Italy, in 1989.

He is currently a Research Scientist with the Italian National Institute of Metrology Research (INRIM), Torino, Italy involved with the maintenance and development of instrumental set-up for magnetic measurements, and the elaboration and characterization of innovative, amorphous, micro- and nano-sized magnetic materials applied as core components in devices of electrotechnics.



**Fausto Fiorillo** received the Laurea degree in physics from the University of Torino, Torino, Italy, in 1972.

He started his career as a Physicist with the Istituto Elettrotecnico Nazionale Galileo Ferraris (now Istituto Nazionale di Ricerca Metrologica - INRIM), in 1974. He has been Research Director with INRIM till retirement, in 2012. He is currently an Emeritus scientist with the same institution. He authored/coauthored some 230 peer-reviewed publications in international scientific journals, review monographs, and chapters on international series on magnetic materials. His

scientific work and research interests include the properties of magnetic materials and their measurement.

Mr. Fiorillo is the author of the comprehensive treatise *Measurement and Characterization of Magnetic Materials* (Academic Press-Elsevier, 2004).



**Marco Storace** (Senior Member, IEEE) was born in Genoa, Italy, in 1969. He received the Laurea (M.Sc.) degree (*Summa Cum Laude*) in electronic engineering and the Ph.D. degree in electrical engineering from the University of Genoa, Genoa, Italy, in 1994 and 1998, respectively.

Since 2011, he has been a Full Professor with the University of Genoa. He was a Visitor with EPFL, Lausanne, Switzerland, in 1998 and 2002. He has authored or coauthored about 180 scientific papers, more than an half of which have been published in international journals. He coauthored *Linear and Nonlinear Circuits: Basic & Advanced Concepts* (2 volumes). His current research interests are in the area of nonlinear circuit theory and applications, analysis and modelling of nonlinear dynamical systems, also networked.

Dr. Storace is a member of the IEEE Technical Committee on Nonlinear Circuits and Systems (TC-NCAS). He served as an Associate Editor of the IEEE TRANSACTIONS ON CIRCUITS AND SYSTEMS – II (2008–2009) and as Chair of the Nonlinear Circuits and Systems Technical Committee (2021–2023).